

JUNE 03 2024

# Feature-based maximum entropy for geophysical properties of the seabed<sup>a)</sup> ✓

D. P. Knobles; William Hodgkiss; Jason Chaytor ; Tracianne Neilsen; Ying-Tsong Lin

 Check for updates

*J. Acoust. Soc. Am.* 155, 3559–3567 (2024)

<https://doi.org/10.1121/10.0026202>




WE BRING THE NOISE,  
YOU BRING THE PRODUCTS

COMMITTED TO A SMARTER,  
MORE CONNECTED FUTURE

 **ETS-LINDGREN**  
An ESCO Technologies Company

## Feature-based maximum entropy for geophysical properties of the seabed<sup>a)</sup>

D. P. Knobles,<sup>1,b)</sup> William Hodgkiss,<sup>2</sup> Jason Chaytor,<sup>3</sup>  Tracianne Neilsen,<sup>4</sup> and Ying-Tsong Lin<sup>2</sup>

<sup>1</sup>Platt Institute of Nuclear Physics, P.O. Box 27200, Austin, Texas 78755, USA

<sup>2</sup>Scipps Institution of Oceanography, University of California at San Diego, La Jolla, California 92093, USA

<sup>3</sup>U.S. Geological Survey, Woods Hole Coastal and Marine Science Center, Woods Hole, Massachusetts 02543, USA

<sup>4</sup>Department of Physics and Astronomy, Brigham Young University, Provo, Utah 84602, USA

### ABSTRACT:

The coherent recombination of a direct and seabed reflected path is sensitive to the geophysical properties of the seabed. The concept of feature-based inversion is used in the analysis of acoustic data collected on a vertical line array (VLA) on the New England continental shelf break in about 200 m of water. The analysis approach for the measurements is based on a ray approach in which a direct and bottom reflected path is recombined, resulting in constructive and destructive interference of the acoustic amplitudes with frequency. The acoustic features have the form of prominent nulls of the measured received levels as a function of frequency as a broadband (500–4500 Hz) source passes the closest point of approach to the VLA. The viscous grain shearing (VGS) model is employed to parameterize a two-layer seabed model. The most likely seabed is a sand sediment with a porosity of about 0.42. There is a possibility of a thin (less than 0.5 m) surface layer having a slightly higher porosity between 0.45 and 0.50. Using the estimates for the VGS parameters inferred from the short-range frequency features, a normal mode model is used to predict the received acoustic levels over larger range scales. © 2024 Acoustical Society of America.

<https://doi.org/10.1121/10.0026202>

(Received 3 January 2024; revised 4 April 2024; accepted 11 May 2024; published online 3 June 2024)

[Editor: James F. Lynch]

Pages: 3559–3567

### I. INTRODUCTION

As part of a larger experiment in May 2022, whose purpose was to characterize the seabed structure on the New England shelf and slope, acoustic recordings were made on a 16-element vertical line array (VLA) during the passage of a towed broadband source. The source tow track and position of the VLA were on the 200 m contour, which is the approximate position of the shelf break. An examination of the time-frequency spectrograms revealed *features* in the form of peaks and nulls in the received intensity time-frequency spectrograms at the closest position of approach (CPA) time. The densities of the peaks and nulls generally increased at the shallower receiver depths. It was ascertained in a pre-analysis of the data that the details of the frequency-dependent acoustic intensity were sensitive to the properties of the seabed, source-receiver range, and depth of the receiver.

The properties of the sound speed profile (SSP) and depth of the source (120 m) permit a statistical inversion of seabed properties using a ray analysis. A finite sediment layer over a basement halfspace are represented by the visco-elastic viscous grain shearing (VGS) model (Buckingham, 2000, 2007). The VGS model parameter

space includes marine sediment properties, such as average porosity, grain bulk modulus, average grain density, and grain size, and several additional parameters that characterize the dynamics of a grain-to-grain contact. The model output is the frequency-dependent sound speed, attenuation, and bulk density, which then allow the complex reflected component of the field to be computed. This paper explores the information content on the geophysical properties of the sediment from frequency features which arise from the coherent combination of the direct and reflected ray components.

The remainder of this paper is organized as follows. Section II discusses the acoustic measurements and Sec. III presents a ray methodology for computing the acoustic field. Section IV presents the VGS model parameterization and prior assumptions. Section V presents the statistical inversion method and Sec. VI presents the results. A conclusion is presented in Sec. VII.

### II. EXPERIMENTAL MEASUREMENTS AND ACOUSTIC FEATURE SELECTION

During Seabed Characterization Experiment (SBCEXP) 2022, the acoustic data were collected on a VLA deployed on the 200 m depth contour near the shelf break. Figure 1 shows the track of the RV Armstrong during the acoustic measurements. The VLA was located at 40.04847° N 70.88417° W. The data of interest are time recordings from

<sup>a)</sup>This paper is part of a special issue on Assessing Sediment Heterogeneity on Continental Shelves and Slopes.

<sup>b)</sup>Email: dpknobles@kphysics.org

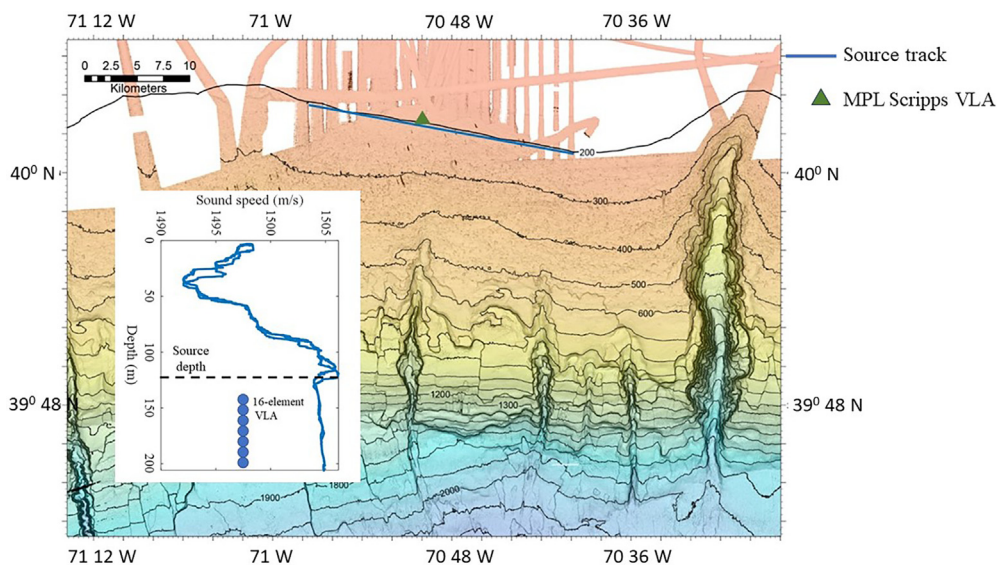


FIG. 1. (Color online) Tow track (blue line), position of VLA (green triangle), and measured SSPs near VLA on the 200 m depth contour on the New England shelf break.

a towed source on Julian day 148 from 1216 to 1800 UTC, which emitted chirp signals in the 500–1250 Hz band, and a second source (on the same tow body and clock), which emitted chirp signals in the 1500–4500 Hz band. The ship speed was about 2.0 kn. The CPA occurred at about 1626 Z, and the CPA range was about 390 m.

SSPs, also displayed in Fig. 1, were derived from a conductivity, temperature, and depth (CTD) measurement near the VLA. Starting at about 120 m, the depth variability of the sound speed is small. For this specific experiment, the placement of the source and receiver mitigates range-dependent effects due to spatial SSP variability.

Time-frequency spectrograms are depicted in Fig. 2(a) for channel 03 and Fig. 2(b) for channel 04, which were processed by short-time Fourier analyses of the recorded time series. The processed spectrograms have a frequency spacing of about 0.19 Hz from 500 to 4500 Hz and a time

spacing of about 8.9 s. At CPA, the peak and null levels in the acoustic intensity are about 110 and 80 dB re  $1 \mu\text{Pa}^2/\text{Hz}$ , respectively.

For this analysis, the frequencies associated with the nulls were selected as *features* because they typically have a smaller uncertainty as compared to the peaks. The frequency spacing between nulls generally became smaller for decreasing receiver depths or equivalently increasing channel numbers. The chirp signal made it difficult to uniquely identify the null frequencies and, hence, is a source of error in the analysis. To mitigate this source of error, there are several considerations. First, the decreasing frequency spacing of nulls with increasing channel number decreases the severity of this source of error. Second, the effects of the Doppler and source aspect were observed to increase with increasing channel number, which caused increasing ambiguity in the position of the nulls. Weighing these considerations, the

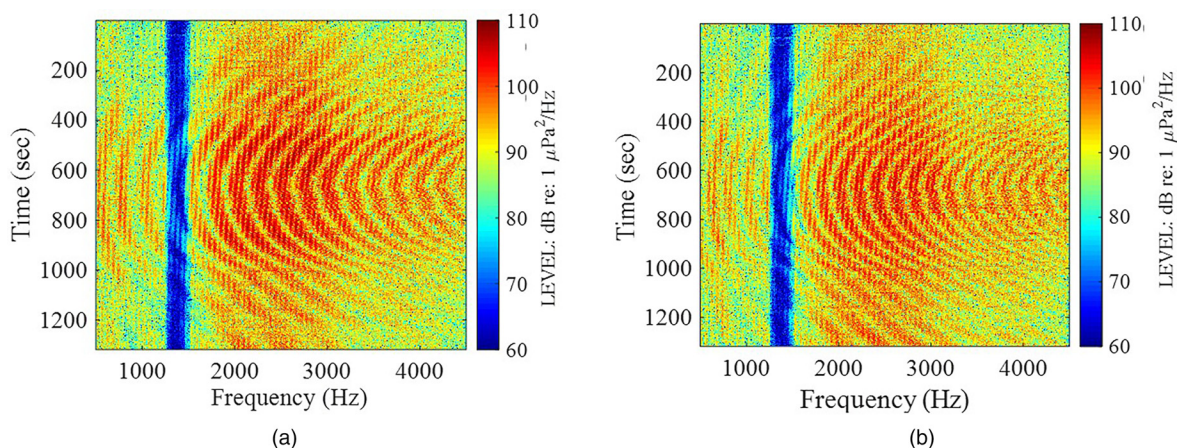


FIG. 2. (Color online) Measured received level as a function of time in the 500–4500 Hz band from a pair of towed sources along the 200 m contour. Data are from VLA (a) channel 03 and (b) channel 04.

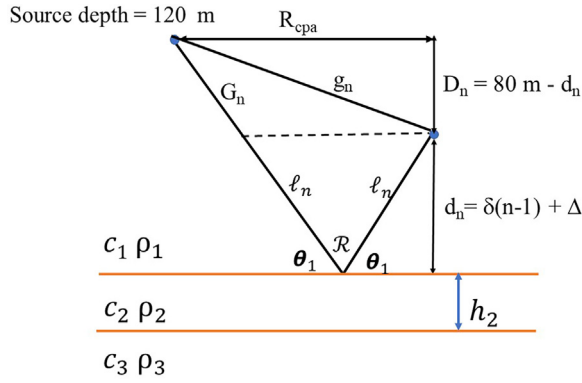


FIG. 3. (Color online) Illustration of ray model that recombines a direct and bottom reflected path at a receiver on the VLA.

smallest error in creating a data sample of null frequencies appeared to be associated with channels 03 and 04.

$$\mathcal{D}_{k=3} = [659\ 905\ 1139\ 1467\ 1635\ 1888\ 2142\ 2390\ 2640\ 2874\ 3121\ 3370\ 3606\ 3866\ 4088\ 4345] \text{ Hz},$$

$$\mathcal{D}_{k=4} = [524\ 718\ 913\ 1106\ 1319\ 1508\ 1709\ 1902\ 2110\ 2295\ 2486\ 2682\ 2882\ 3090\ 3275\ 3469\ 3673\ 3868\ 4059\ 4281\ 4486] \text{ Hz}.$$

Section VI will show the results of the statistical inference for seabed parameters using these two data samples and then apply the estimates to predict the frequency nulls for other channel numbers, specifically channel 02 and 05.

### III. RAY ANALYSIS APPROACH

The SSP and source depth combined with the position of the VLA affords an opportunity to analyze the data using a ray analysis as depicted in Fig. 3. The reflection coefficient,  $\mathcal{R}$ , is a total plane wave reflection coefficient that includes specular reflection at the water sediment interface and all multiple reflection within the  $h_2$  layer.

For each sampling of the multidimensional seabed parameter space shown in Table I, the acoustic pressure at

TABLE I. Parameter space,  $\mathcal{H}$ , with upper and lower bounds. The space is sampled using Monte Carlo sampling.

Parameter	Symbol	Units	Upper	Lower
Porosity in layer 2	$\phi_2$	—	0.37	0.75
Layer thickness layer 2	$h_2$	m	0.01	1
Grain bulk modulus layer 2	$K_{g2}$	GPa	15	50
Strain hardening index layer 2	$n_2$	—	0.05	0.12
log of viscous time constant layer 2	$\log(\tau_2/1 \text{ s})$	—	-4.0	4.0
Porosity in layer 3	$\phi_3$	—	0.37	0.75
Grain bulk modulus layer 3	$K_{g3}$	GPa	15	50
Strain hardening index layer 3	$n_3$	—	0.05	0.12
Log of viscous time constant layer 3	$\log(\tau_3/1 \text{ s})$	—	-4.0	4.0
CPA range	$R_{\text{cpa}}$	m	350	400

the  $k$ th receiver for a direct and bottom reflected path with a source level,  $S_0$ , is

$$P = \frac{S_0}{4\pi} (\mathcal{R}e^{i\xi_1}) / (G_n + 2\ell_n) + e^{i\xi_2} / g_n, \quad (1)$$

where

$$\xi_1 = \frac{2\pi f}{c_1} (G_n + 2\ell_n) \quad (2)$$

and

$$\xi_2 = \frac{2\pi f}{c_1} (g_n). \quad (3)$$

The seabed reflection coefficient for the seabed model in Fig. 3 is

$$\mathcal{R}(\theta_1, \omega) = \frac{R_{12} + R_{23}e^{2iF_2}}{1 + R_{12}R_{23}e^{2iF_2}}, \quad (4)$$

where

$$F_2 = k_2 h_2 \sin(\theta_2), \quad (5)$$

and  $R_{12}$  and  $R_{23}$  are the Raleigh reflection coefficients at interfaces 12 and 23. The specific forms of  $R_{12}$  and  $R_{23}$  are

$$R_{12} = \frac{\rho_2 C_2 \sin(\theta_1) - \rho_1 c_1 \sin(\theta_2)}{\rho_2 C_2 \sin(\theta_1) + \rho_1 c_1 \sin(\theta_2)} \quad (6)$$

and

$$R_{23} = \frac{\rho_3 C_3 \sin(\theta_2) - \rho_2 C_2 \sin(\theta_3)}{\rho_3 C_3 \sin(\theta_2) + \rho_2 C_2 \sin(\theta_3)}. \quad (7)$$

The complex sound speeds in layers 2 and 3 are

$$C_2 = c_2(f) + \frac{i}{2\pi} (\alpha_2(f)/8.686)/f \quad (8)$$

and

$$C_3 = c_3(f) + \frac{i}{2\pi} (\alpha_3(f)/8.686)/f, \quad (9)$$

where  $\alpha_2$  and  $\alpha_3$  have units of dB/m. Also, the acoustic wavenumber in layer 2 is

$$k_2 = \frac{2\pi f}{C_2}, \quad (10)$$

and  $f$  is the acoustic frequency.  $\mathcal{R}$  is frequency dependent because of the finite thickness of the top sediment layer and the frequency dispersion of the complex sound speed in layers 2 and 3. The acoustic received level is

$$\text{RL} = -20 \log(4\pi|P|). \quad (11)$$

The frequencies where  $\text{RL}(f)$  become nulls are the modeled frequencies,  $M_{k,n}$ , where  $k$  is channel number and  $n = 1, 2, \dots, N_k$

counts how many nulls are found on receiver  $k$ . The expression in Eq. (4) can easily be extended to the case for a stack of finite layers (Jensen *et al.*, 2011).

#### IV. SEABED MODEL PARAMETERIZATION

The seabed model, depicted in Fig. 4, assumes a sediment layer of finite thickness,  $h_2$ , overlying a halfspace. Each sediment layer is parameterized in terms of the geophysical parameters in the VGS model (Buckingham, 2000, 2007). The compressional sound speed and attenuations in both layers, which are input into a normal mode model, are computed from the VGS model. The first sediment layer allows for a frequency-dependent response that can occur when the acoustic wavelength is on the order of a layer thickness.

The selection of a seabed model is based on a variety of factors, including model accuracy, the ability to describe a wide class of sediments such as those characterized by the Wentworth scale (Wentworth, 1922), and the ability to determine model parameter values without overfitting the data (Goodfellow *et al.*, 2016). A useful form of a seabed model is one that obeys causality. Causal models restrict the frequency dispersion of the sound speed and attenuation to a Kramers–Kronig relationship (Toll, 1956; Jackson, 1975), which acts to reduce the dimensionality of the parameter space. Examples of such causal models include viscoelastic models such as the silt suspension (Brown *et al.*, 2020) and VGS formulations. Another class of causal models are poro-elastic models, which assume a sediment frame with pore water between the sediment structure. Such examples include the Biot-Stoll model (Biot, 1956, 1962; Stoll, 2002) and variants such as the Biot-squirt model (Kimura, 2011). These models are plagued by a large number of parameters whose values are difficult to determine and, as such, are susceptible to overfitting data. Another issue with poro-elastic models is that they typically are not valid for soft sediments. Chotiros (2021) has attempted to correct this issue by introducing a poro-elastic model for mud. Again, the issue with such extensions of a poro-elastic model lies with the large number of unknown parameters. In contrast, the VGS model is based on a simple version Zener model (Carcione, 2014) with a mechanical framework consisting

of a Hookean spring and Newtonian dashpot. This lends itself to a modicum number of parameters and, as such, are less susceptible to overfitting data as compared to viscoelastic models.

The parameterization of the VGS model for the sediment layer and halfspace includes  $\phi$ ,  $u_g$ ,  $\rho_g$ ,  $K_g$ ,  $K_b$ ,  $\rho_b$ ,  $n$ ,  $\tau$ ,  $\gamma_p$ , and  $\gamma_s$ , which are the porosity, grain size, grain density, grain bulk modulus, bulk modulus, bulk density, strain hardening index, viscous time constant, compressional modulus, and shear modulus, respectively. Several parameters may be viewed as dependent parameters. For example,

$$u_g(N) = 2\Delta(2B - 1)/(1 - B), \tag{12}$$

where  $\phi_{\min} = 0.37$  and  $\Delta = 1 \mu\text{m}$ . Also, the Wood-Mallock equations (Wood, 1930; Mallock, 1910) afford an estimate of  $\rho_b$  in terms of  $\rho_g$ ,  $\phi$ , and the density of the water,  $\rho_w$ ,

$$\rho_b(\phi) = \rho_g(\phi) + \phi(\rho_w - \rho_g), \tag{13}$$

where  $\rho_w$  is the density of the pore water. Also, an estimate of  $K_b$  can be inferred from

$$\frac{1}{K_b} = \frac{\phi}{K_w} + \frac{1 - \phi}{K_g}, \tag{14}$$

where  $K_w$  is the water bulk modulus. It is assumed that  $K_w$  and  $\rho_w$  are known with values of  $2.395 \times 10^9 \text{ Pa}$  and  $1023 \text{ kg/m}^3$ , respectively. It is also assumed that  $\gamma_p$  and  $\gamma_s$  are known with values of  $3.734 \times 10^8 \text{ Pa}$  and  $2.172 \times 10^7 \text{ Pa}$ , respectively (Buckingham, 2005).

Table I shows the parameter space for the two-layer model, which includes the assumed upper and lower parameter bounds. The upper and lower bounds for  $\phi$  are representative of a soft clay and a very coarse sand or granules, respectively. Also, the upper and lower bounds for the grain bulk modulus are representative of a very coarse sand and a soft sediment, respectively. However, there is significant uncertainty in correlating values of the  $K_{g3}$  to sediment classification. As the sediment sound speed is highly sensitive to  $K_{g3}$ , one can expect that there will be parameter correlations between  $K_{g3}$  and  $\phi_3$ . The upper bound for  $n$  in Table I assumes that for a very hard sand,  $n$  is slightly higher than the value of  $n = 0.085$ , which was derived by Buckingham (2005) for a fine to medium sand sediment. Similarly, for a lower bound of  $n$ , a value of 0.05 is used because a previous study for mud sediments suggested a value of 0.06 (Knobles *et al.*, 2021).

In the VGS theory, the effects of viscosity are introduced in terms of  $\tau$ . From the analysis of experiments for sandy sediments, Buckingham (2005) determined a value of  $\tau$  to be about 0.00012 s or  $\log(\tau/1 \text{ s}) = -3.9208$ . This value reproduces the observed transition frequency in which the attenuation exponent transitions from a value of two to a value of 1/2 for data taken in medium sand. It was observed that this value of  $\tau$  fits the reported attenuations from experiments in the Yellow Sea (fine to medium sand; Zhou *et al.*, 1987) and a medium to coarse sand observed on a sand sheet

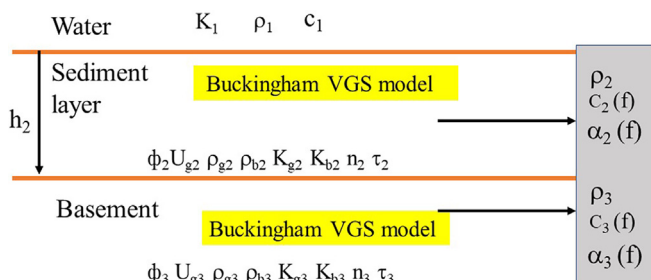


FIG. 4. (Color online) A three-layer model for reflection of sound from the seabed. Layers 1 and 3 are halfspaces.  $c_1$ ,  $c_2$ , and  $c_3$  are the real components of the sound speed in layers 1–3. Layer 2 has a finite sediment thickness,  $h_2$ , and layer 3 is a sediment halfspace. Layers 2 and 3 are characterized by geophysical and grain contact parameters within the VGS model.

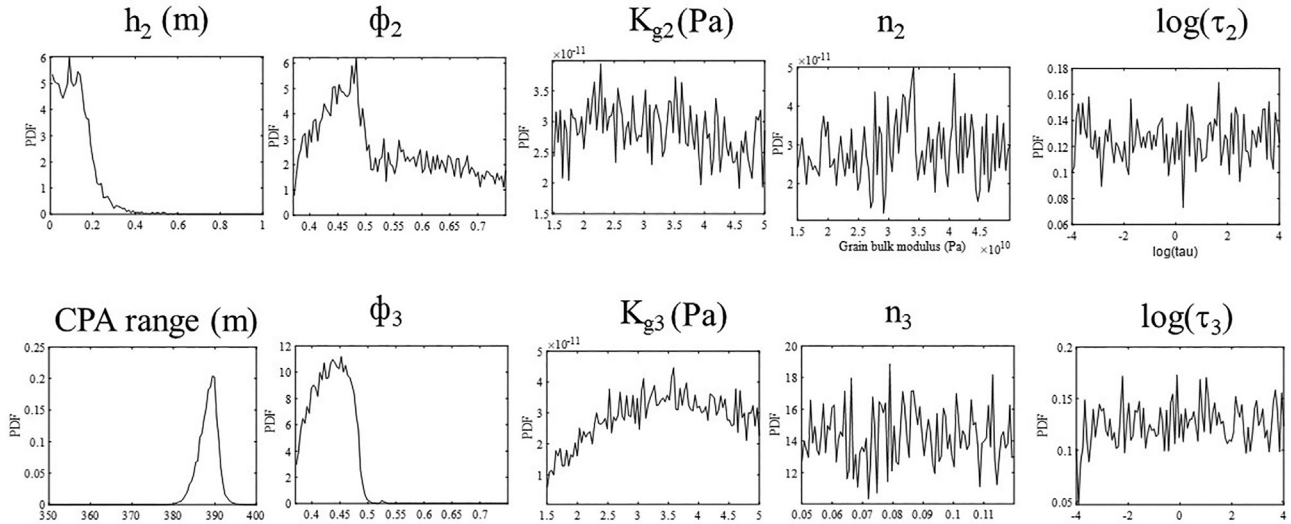


FIG. 5. Marginal pdfs derived from the posterior canonical distribution.

on the New Jersey continental shelf (Knobles *et al.*, 2008) and, more generally, the attenuation of the group of experimental data reported by Zhou *et al.* (2009). If  $\log(\tau/1 \text{ s})$  is set to a large value ( $\log(\tau/1 \text{ s}) = 4.0$ ; grain shearing limit of VGS), the dispersion of the sound speed is very weak, which is consistent with the clayey sandy silt sediment studied during SBCEXP 2017 and other experiments with low-speed seabeds (Wilson *et al.*, 2020; Boyles, 1997).

A cautionary note is that estimates for  $\tau(N)$  for a sand sediment do not simultaneously fit reported values for sound speed and attenuation dispersion over the 10 Hz to  $1 \times 10^6$  Hz band. For example, Chotirous and Isakson (2012) have shown that sound speed and attenuation dispersion of the SAX99 data can be well fit using a variant of the Biot model. In contrast, the VGS model, while doing a *good* job of fitting the attenuation, predicts sound speed ratio values that fall slightly below the data for  $f > 5$  kHz. This is likely not a serious concern in this study because the bandwidths of the processed data are 500–4500 Hz.

V. STATISTICAL INVERSION METHOD

The inverse problem requires an error function that compares the measured frequencies and modeled

TABLE II. Optimal, average, and standard deviations of parameter values from pdfs.

Parameter	Units	$\hat{\mathcal{H}}$	$E[X]$	$\sigma$
$\phi_2$	—	0.48	0.53	0.10
$h_2$	m	0.32	0.12	0.08
$K_{g2}$	GPa	31.56	32.0	10.0
$n_2$	—	0.12	0.085	0.021
$\phi_3$	—	0.42	0.43	0.03
$K_{g3}$	GPa	26.34	34.1	9.2
$n_3$	—	0.071	0.085	0.020
CPA range	m	388.3	388.3	2.3
$\log(\tau_2)$	—	-3.28	0.02	2.3
$\log(\tau_3)$	—	3.4665	0.08	2.3

frequencies. For the problem at hand, we chose the error function to have the form

$$E(\mathcal{H}) = \sum_{k=3}^4 E_k(\mathcal{H} : \mathcal{D}_k), \tag{15}$$

where

$$E_k(\mathcal{H} : \mathcal{D}_k) = \sum_{n=1}^{N_k} (\mathcal{D}_{k,n} - M_{k,n}(\mathcal{H}))^2, \tag{16}$$

where  $J(k)$  is the number of null frequencies for receiver,  $k$ , and the parameter space is

$$\mathcal{H} = [\phi_2, \phi_3, h_2, n_2, n_3, K_{g2}, K_{g3}, \tau_2, \tau_3, R_{cpa}]. \tag{17}$$

The ensemble maximum entropy method (Knobles *et al.*, 2012) employed in this analysis is defined by a *canonical* distribution,

$$\mathcal{P}(\mathcal{H} | \mathcal{D}_k, M) = \mathcal{P}(\mathcal{H}, M) \frac{\exp[-\beta_k E_k(\mathcal{H}, \mathcal{D}_k)]}{Z_k}, \tag{18}$$

where  $Z_k$  and  $\beta_k$  are the partition function and Boltzmann factor, respectively, with

$$Z_k = \int d\mathcal{H} \mathcal{P}(\mathcal{H}, M) \exp[-\beta_k E_k(\mathcal{H}, \mathcal{D}_k)]. \tag{19}$$

Jaynes (1957a,b) first introduced the concept of maximum entropy, which is rooted in statistical mechanics.

TABLE III. Optimal values for sound speed and attenuation in layer 3 in 0.50–4.5 kHz band.

Frequency (Hz)	500	1000	1500	2000	2500	3000	3500	4000	4500
Sound speed ratio	1.071	1.077	1.079	1.081	1.082	1.082	1.082	1.082	1.083
Attenuation (dB/m)	0.160	0.274	0.340	0.392	0.444	0.485	0.528	0.571	0.614

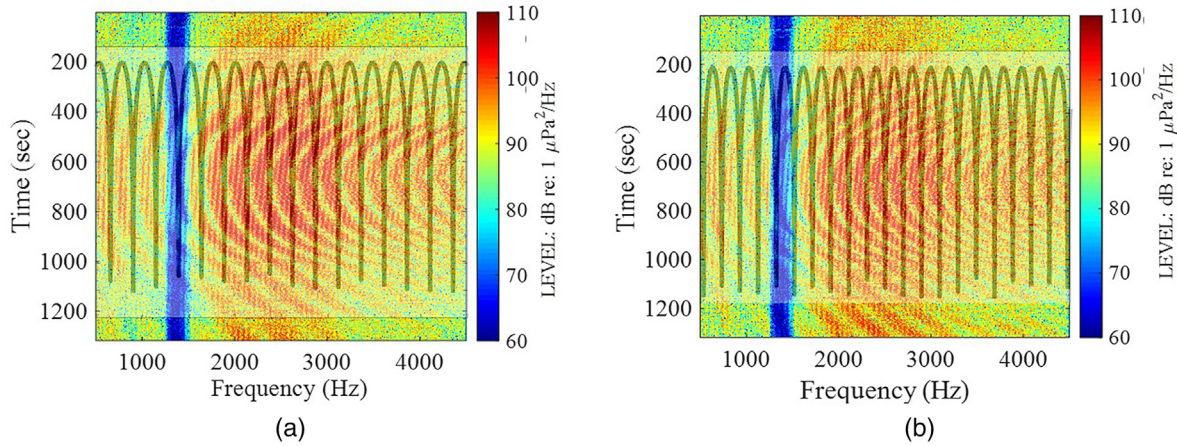


FIG. 6. (Color online) Comparison of measured and ray results for (a) channel 03 and (b) channel 04. The ray model (black line) results are received level (vertical axis) at CPA time and have been superimposed on top of the measured spectrogram. The model results are for the optimal solution.

The specific development of the form of maximum entropy used in the current analysis is called relative maximum entropy (Kullback and Leibler, 1951; Bilbro and Van den Bout, 1992; Tishby *et al.*, 1989). The details of determining the Boltzmann factor,  $\beta_k$ , in Eq. (18) have been previously reported in Knobles *et al.* (2012).

### VI. RESULTS

The parameter space,  $\mathcal{H}$ , is randomly sampled, and marginal probability density functions (pdfs) are calculated for  $\phi_2$ ,  $h_2$ ,  $K_{g2}$ ,  $n_2$ ,  $\tau_2$ ,  $\phi_3$ ,  $K_{g3}$ ,  $n_3$ ,  $\tau_3$ , and  $R_{cpa}$  and displayed in Fig. 5. Table II shows optimal values and average and standard deviations from the marginal pdfs. The optimal value is  $\hat{\mathcal{H}}$  where  $\hat{\mathcal{H}} \in \mathcal{H}$  such that  $E(\hat{\mathcal{H}}) \leq E(\mathcal{H})$  for all  $\mathcal{H}$ . The expected and standard deviations for the values of a parameter,  $X$ , are computed using the marginal,  $P_X$ , as

$$\mu = E[X] = \int dxXP_X(x), \quad (20)$$

$$\sigma = \int dx\sqrt{(\mu - x)^2P_X(x)}. \quad (21)$$

The pdf for  $h_2$  does not have a Gaussian-like shape but rather has its largest values from about 0 to 0.2 m, and then rapidly decreases to zero at a thickness of about 0.4 m. An estimate of the thickness from Table II suggests that the first layer has thickness of less than or equal to 0.20 m. The pdf for  $\phi_2$  has a broad peak centered at a value at about 0.45, which is a fine sand classification. The long tail of the pdf causes the average value to exceed 0.50. The pdfs for  $K_{g2}$ ,  $n_2$ , and  $\tau_2$  are essentially flat, i.e., they convey no information about the parameter values. The pdf for  $\phi_3$  has a broad peak centered around 0.43, which has a classification of fine sand. The average value and peak value of the pdf have about the same value. The pdfs for  $n_3$  and  $\tau_3$  are approximately flat, however, the pdf for  $K_{g3}$  suggests that  $K_{g3} > 25$  GPa. The pdf for the CPA range has a sharp peak at about 388 m, which is consistent with the experimental measurement.

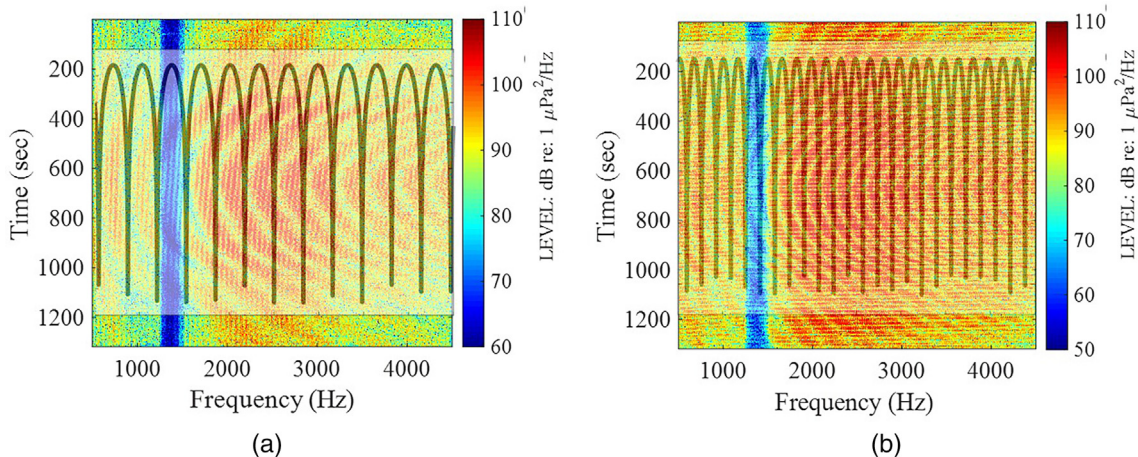


FIG. 7. (Color online) Comparison of measured and ray results for (a) channel 02 and (b) channel 05. The ray model (black line) results are received level (vertical axis) at CPA time and have been superimposed on top of the measured spectrogram. The model results are for the optimal solution.

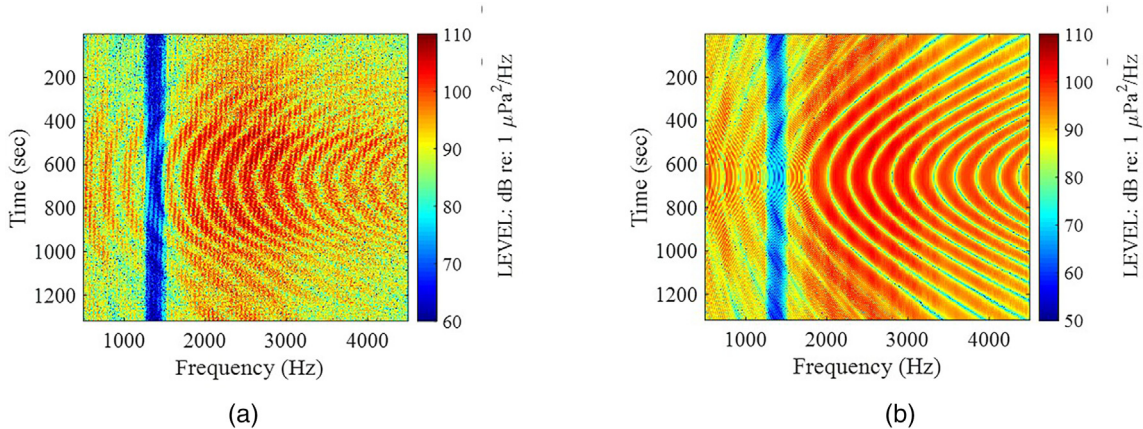


FIG. 8. (Color online) Comparison of received spectrogram for (a) measured and (b) normal mode model results for channel 03.

The optimal parameter values for  $\mathcal{H}$  from Table II are used to compute the sediment sound speeds, attenuations, and bulk densities, which are then used by the ray model to predict the received levels at CPA. Table III shows, for example, the predicted sediment sound speeds and attenuations in the 500–4500 Hz processing band for layer 3. Figure 6 depicts a comparison of the ray theory results with the measured spectrograms for channels 03 and 04. The nulls of the ray theory prediction of the acoustic intensity for channels 03 and 04 are in *good* agreement with the observed null frequencies. The optimal values for  $\mathcal{H}$  from Table II were also used to compute the ray model at CPA for the data samples not used in the optimization, specifically, feature frequencies extracted from channels 02 and 05. Figure 7 displays a comparison of the ray theory results with the measured spectrograms for channels 02 and 05. The nulls of the ray theory prediction of the acoustic intensity for channels 02 and 05 are qualitatively in *good* agreement with the observed null frequencies.

Figures 8 and 9 compare the measured spectrograms with the modeled spectrograms produced by a normal mode algorithm (Westwood *et al.*, 1996) that uses optimal values for  $\mathcal{H}$  from Table II for channels 03 and 04, respectively. The model source levels are those from the implicit formulation (Tollefsen *et al.*, 2022; Knobles, 2015). The assumed

ship speed was the reported speed of the tow ship (2.0 kn). It is important to note that the measured striation pattern is not fully symmetric about the CPA range, which may be ascribed to an unknown range dependence along the track, or nonuniform speed and source level, or a combination of all these factors.

The seabed parameters inferred using data at short ranges can be used to make predictions at significantly longer ranges. An example is shown in Fig. 10 which compares the measured spectrogram with the modeled spectrograms produced by a normal mode algorithm that uses optimal values for  $\mathcal{H}$  from Table II for channel 03. Qualitatively, the modeled and measured received levels over the 10.5 km range scale are in agreement. However, at the longer ranges, the data do not possess the time-frequency coherent striations predicted in the simulated spectrogram. This comparison suggests the existence of an unknown mechanism that causes a loss of coherence in the acoustic field with increasing range.

## VII. CONCLUSIONS

A SBCEXP was performed at the New England shelf-break. The experimental setup afforded an acoustic ray analysis method with the recombination of the direct and bottom

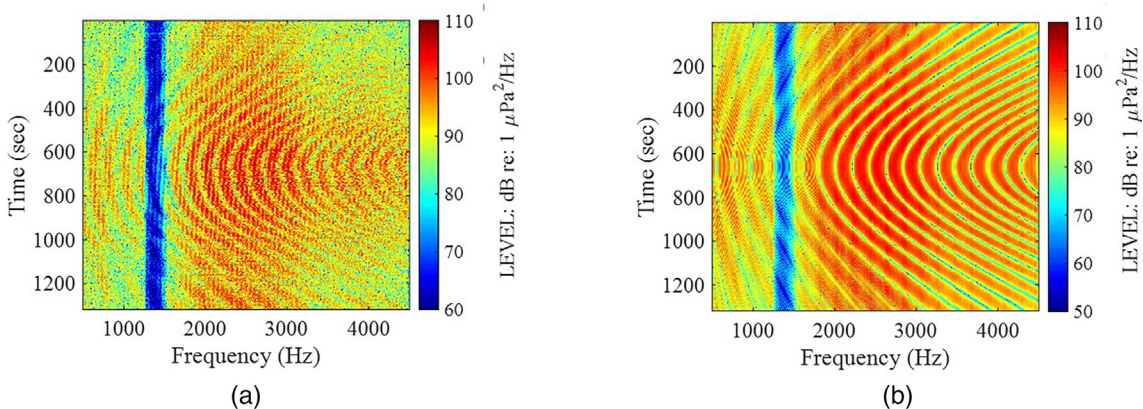


FIG. 9. (Color online) Comparison of received spectrogram for (a) measured and (b) normal mode model results for channel 04.



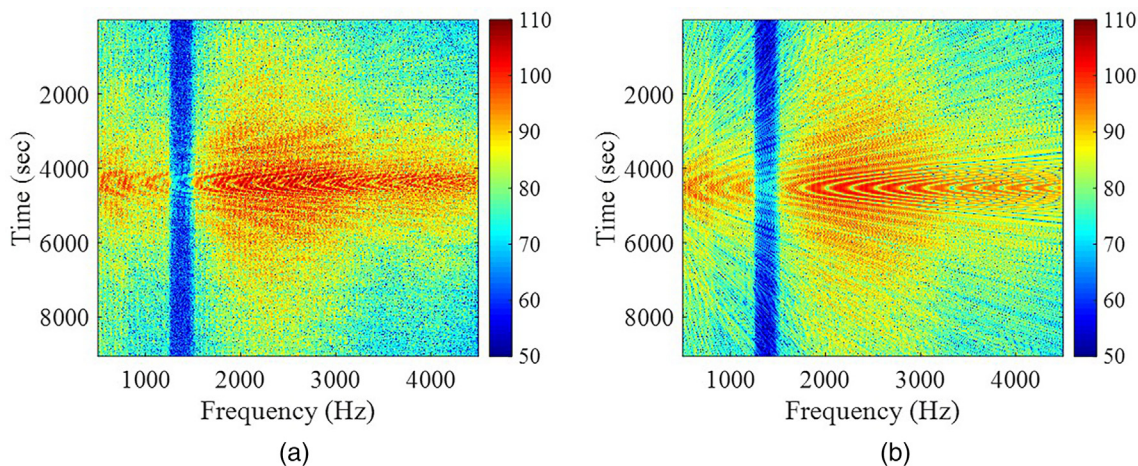


FIG. 10. (Color online) Received spectrogram for (a) measured and (b) normal mode model results for channel 03 on a larger range scale.

reflected paths. The analysis introduced concepts that included feature-based inversion and model dimensional reductions. This feature-based inversion identifies a unique feature in the acoustic field and then formulates a statistical approach to infer parameter values for a seabed model.

The concepts were applied to a statistical analyses of chirp tow data in the 500–4500 Hz band. Estimates of parameter values for the porosity, grain bulk modulus, strain hardening index, and viscous time constant were made for two sediment layers. The resulting probability density indicates that the most probable characterization of the seabed is a thin (<0.2 m) sand layer over a thicker amount of sand. The optimal inferred seabed model using acoustic measurements made at a range of about 390 m was successfully employed to predict the received acoustic levels over a range scale of about 10.5 km. However, there appears to be an unknown mechanism that causes a loss of intensity striations in the time/range frequency with increasing range.

## ACKNOWLEDGMENTS

This work was supported by the Office of Naval Research, Contract No.00014-22-1-2172.

## AUTHOR DECLARATIONS

### Conflict of Interest

The authors have no conflicts to disclose.

## DATA AVAILABILITY

The data that support the findings of this study are available from W.H.

Bilbro, G. L., and Van den Bout, D. E. (1992). "Maximum entropy and learning theory," *Neural Comput.* **4**(6), 839–853.  
 Biot, M. A. (1956). "Theory of propagation of elastic waves in a fluid-saturated porous solid. II. Higher frequency range," *J. Acoust. Soc. Am.* **28**(2), 179–191.  
 Biot, M. A. (1962). "Generalized theory of acoustic propagation in porous dissipative media," *J. Acoust. Soc. Am.* **34**, 1254–1264.

Boyles, F. A. (1997). "Observations on attenuation and shear-wave velocity in fine-grained, marine sediments," *J. Acoust. Soc. Am.* **101**(1), 3385–3397.  
 Brown, E. M., Lin, Y. T., Chaytor, J. D., and Siegmund, W. L. (2020). "Geoacoustic inversion for a New England mud patch sediment using the silt-suspension theory of marine md," *IEEE J. Ocean. Eng.* **45**(1), 144–160.  
 Buckingham, M. J. (2000). "Wave propagation, stress relaxation, and grain-to-grain shearing in saturated, unconsolidated marine sediments," *J. Acoust. Soc. Am.* **108**(6), 2796–2815.  
 Buckingham, M. J. (2005). "Compressional and shear wave properties of marine sediments: Comparisons between theory and data," *J. Acoust. Soc. Am.* **117**(1), 137–152.  
 Buckingham, M. J. (2007). "On pore-fluid viscosity and the wave properties of saturated granular materials including marine sediments," *J. Acoust. Soc. Am.* **136**(5), 2478–2488.  
 Carcione, J. M. (2014). *Wave Fields in Real Media: Wave Propagation in Anisotropic, Anelastic, Porous and Electromagnetic Media*, 3rd ed. (Elsevier Science, Amsterdam, Netherlands), Chap. 2.  
 Chotiros, N. P. (2021). "A porous medium model for mud," *J. Acoust. Soc. Am.* **149**(1), 629–644.  
 Chotiros, N. P., and Isakson, M. J. (2012). "The evolution of sediment acoustic models," *AIP Conf. Proc.* **1495**, 193–201.  
 Goodfellow, I., Bengio, Y., and Courville, A. (2016). *Deep Learning* (MIT Press, Cambridge, MA), Chap. 4.  
 Jackson, J. D. (1975). *Classical Electrodynamics*, 2nd ed. (Wiley, New York), Chap. 7.10.  
 Jaynes, E. (1957a). "Information theory and statistical mechanics," *Phys. Rev.* **106**(4), 620–630.  
 Jaynes, E. (1957b). "Information theory and statistical mechanics II," *Phys. Rev.* **108**(2), 171–190.  
 Jensen, F., Kuperman, W., Porter, M., and Schmidt, H. (2011). *Computational Ocean Acoustics*, 2nd ed. (Springer, New York), Chap. 2.  
 Kimura, M. (2011). "Velocity dispersion and attenuation in granular marine sediments: Comparison of measurements with predictions using acoustic models," *J. Acoust. Soc. Am.* **129**, 3544–3561.  
 Knobles, D. P. (2015). "Maximum entropy inference of seabed attenuation parameters using ship radiated broadband noise," *J. Acoust. Soc. Am.* **138**(3), 3563–3575.  
 Knobles, D. P., Escobar, C., Buckingham, M. J., Hodgkiss, W. A., Wilson, P. S., Neilsen, T. B., and Badiely, M. (2021). "Statistical inference of the frequency dependence of the phase speed and attenuation of an acoustic wave in a fine-grained marine sediment," *IEEE J. Ocean. Eng.* **47**(3), 553–564.  
 Knobles, D. P., Sagers, J., and Koch, R. A. (2012). "Maximum entropy approach for statistical inference in an ocean acoustic waveguide," *J. Acoust. Soc. Am.* **131**(2), 1087–1101.  
 Knobles, D. P., Wilson, P. S., Goff, J. A., and Cho, S. E. (2008). "A seabed acoustics experiment on a sand ridge on the New Jersey continental shelf," *J. Acoust. Soc. Am.* **124**, EL151–EL156.  
 Kullback, S., and Leibler, R. A. (1951). "On information and sufficiency," *Ann. Math. Statist.* **22**(1), 79–86.

- Mallock, A. (1910). "The damping of sound by frothy liquids," *Proc. R. Soc. London, Ser. A* **84**(572), 391–395.
- Stoll, R. D. (2002). "Velocity dispersion in water-saturated granular sediments," *J. Acoust. Soc. Am.* **111**(2), 785–793.
- Tishby, N., Levin, E., and Solla, S. A. (1989). in *International Joint Conference on Neural Networks (IJCNN)*, Washington, DC (IEEE, New York), pp. 403–410.
- Toll, J. S. (1956). "Causality and the dispersion relation: Logical foundations," *Phys. Rev.* **104**, 1760–1770.
- Tollefsen, D., Hodgkiss, S. E., Dosso, S., Bonnel, J., and Knobles, D. P. (2022). "Probabilistic estimation of merchant ship source levels in an uncertain shallow-water environment," *IEEE J. Ocean. Eng.* **47**(3), 647–665.
- Wentworth, C. (1922). "A scale of grade and class terms for clastic sediments," *J. Geol.* **30**(5), 377–392.
- Westwood, E. K., Tindle, C. T., and Chapman, N. R. (1996). "A normal mode model for acousto-elastic ocean environments," *J. Acoust. Soc. Am.* **100**, 3631–3645.
- Wilson, P. S., Knobles, D. P., and Neilsen, T. A. (2020). "Guest editorial An overview of the seabed characterization experiment," *IEEE J. Ocean. Eng.* **45**(1), 1–13.
- Wood, A. B. (1930). *A Textbook of Sound* (MacMillan, New York), Chap 2.
- Zhou, J. X., Zhang, X. Z., and Knobles, D. P. (2009). "Low frequency geoacoustic model for the effective properties of sandy sea bottoms," *J. Acoust. Soc. Am.* **125**, 2847–2866.
- Zhou, J. X., Zhang, X. Z., and Rogers, P. H. (1987). "Effect of frequency dependence of sea-bottom attenuation on the optimum frequency for acoustic propagation in shallow water," *J. Acoust. Soc. Am.* **82**(2), 287–292.